Inorganic Chemistry

pubs.acs.org/IC Article

Metal Sulfide Ion Exchangers: High Acid Stability of $Na_{2x}Mg_{2y-x}Sn_{4-y}S_8$ (NMS) and Topotactic Conversion to 2D Solid Acids with Semiconducting Character

Michael A. Quintero,[‖] Anastasia D. Pournara,[‖] Richard Godsel, Zhi Li, Shobhana Panuganti, Xiuquan Zhou, Christopher Wolverton, and Mercouri G. Kanatzidis*

Cite This: *Inorg. Chem.* 2023, 62, 15971−15982 Read Online

ACCESS | Metrics & More | Article Recommendations | Supporting Information

ABSTRACT: Metal sulfide ion exchange materials (MSIEs) are of interest for nuclear waste remediation applications. We report the high stability of two structurally related metal sulfide ion exchange materials, $Na_{2x}Mg_{2y-x}Sn_{4-y}S_8$ (Mg-NMS) and Na_2SnS_3 (Na-NMS), in strongly acid media, in addition to the preparation of $Na_{2x}Ni_{2y-x}Sn_{4-y}S_8$ (Ni-NMS). Their formation progress during synthesis is studied with in-situ methods, with the target phases appearing in <15 min, reaction completion in <12 h, and high yields (75−80%). Upon contact with nitric or hydrochloric acid, these materials topotactically exchange Na^+ for H^+, proceeding in a stepwise protonation pathway for $Na_{5.33}Sn_{2.67}S_8$. Na-NMS is stable in 2 M HNO_3 and Mg-NMS is stable in 4 M HNO_3 for up to 4 h, while both NMS materials are stable in 6 M HCl for up to 4 days. However, the treatment of Mg-NMS and Na-NMS with 2−6 M H_2SO_4 reveals a much slower protonation process since after 4 h of contact both NMS and HMS are present in the solution. The resultant protonated materials, $H_{2x}Mg_{2y-x}Sn_{4-y}S_8$ and $H_{4x}[(H_yNa_{y-1})_{1.33x}Sn_{4-1.33x}]S_8$, are themselves solid acids and readily react with and intercalate a variety of organic amines, where the band gap of the resultant adduct is influenced by amine choice and can be tuned within the range of 1.88(5)−2.27(5) eV. The work function energy values for all materials were extracted from photoemission yield spectroscopy in air (PYSA) measurements and range from 5.47 (2) to 5.76 (2) eV, and the relative band alignments of the materials are discussed. DFT calculations suggest that the electronic structure of $Na_2MgSn_3S_8$ and $H_2MgSn_3S_8$ makes them indirect gap semiconductors with multi-valley band edges, with carriers confined to the $[MgSn_3S_8]^{2-}$ layers. Light electron effective masses indicate high electron mobilities.

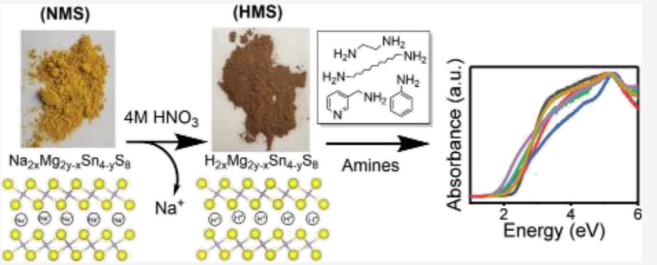

INTRODUCTION

Spent fuel rods, made of uranium and fission byproducts, are the largest waste from nuclear power generation. They are either stored or reprocessed, with the most common method being the plutonium uranium reduction extraction (PUREX) using tributyl phosphate (TBP).[1] However, this method generates large amounts of liquid waste and tends to form emulsions which exhibit extraction efficiency, leading to the pursuit of alternative solid-phase extractants. Solid phase extractants offer benefits over organic solvents in reprocessing,[2] with faster kinetics[3] and no risk of emulsions. Materials like functionalized silica,[4] polymer resins,[5] and metal oxides[6] show promise in separating actinides from nitric acid with high selectivity, but have limitations in stability for harsh conditions. Layered metal sulfides are a promising, emerging class of materials for actinide separation yet to be studied under harsh conditions.[7] These issues are the motivation for the work reported here.

Metal sulfide ion exchangers (MSIEs) comprise a relatively new class of ion exchange materials that exploit the selectivity of soft Lewis basic S^{2-} ligands for the capture of both heavy metals and ions found in nuclear waste.[7] Because their sequestration method relies on forming bonds between sulfur and the analytes of interest, they intrinsically have a low affinity for hard Lewis acid ions such as Na^+, K^+, Ca^{2+}, and others. Previous studies have demonstrated high removal efficiencies of Hg^{2+}, Pb^{2+}, Cd^{2+}, Ni^{2+}, Co^{2+}, UO_2^{2+}, Cs^+, and Sr^{2+} over a wide range of pH values (1 < pH < 12).[8−24] In particular, among the reported MSIEs, $K_2MnSn_2S_6$ (KMS-1)[13] and $KInSnS_4$ (InSnS-1)[25] have demonstrated selectivity in strongly acid solutions as well. These qualities make MSIEs promising candidates for use in the capture of actinides from aqueous solutions. However, the stability and performance of these

Received: June 21, 2023
Published: September 18, 2023

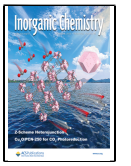

materials under harsh conditions relevant to the reprocessing of nuclear fuel are yet to be studied.

Herein, we describe three MSIE materials: $Na_{2x}Mg_{2y-x}Sn_{4-y}S_8$ (Mg-NMS), Na_2SnS_3[26] (Na-NMS), and $Na_{2x}Ni_{2y-x}Sn_{4-y}S_8$ (Ni-NMS). The three materials, referred to as NMS, exhibit layered two dimensional (2D) structures with Na^+ ions between the layers with high acid stability. In order to place all materials on an iso-formulaic basis, we will refer to Na_2SnS_3 as $Na_4[Na_{1.33}Sn_{2.67}]S_8$ which is stoichiometrically equivalent. We find that Mg-NMS and Na-NMS materials are notably stable in hydrochloric acid, retaining crystallinity for 4 days even in 6 M HCl solutions, while they exhibit satisfactory stability in solutions up to 4 M of nitric acid. Upon submersion in acid, the materials quickly ion-exchange for H^+ in solution forming the solid acids $H_{2x}Mg_{2y-x}Sn_{4-y}S_8$ and $H_4[(H_yNa_{y-1})_{1.33}Sn_{2.67}]S_8$. The protonated materials retain their layered crystal structure, and they are novel solid acids which are consistent with their reactivity toward basic amines which engage in acid−base reactions and easily intercalate between the layers. Finally, these materials are also interesting quasi-2D semiconductors on their own. Using DFT calculations, we analyzed the electronic structure of $Na_2MgSn_3S_8$ and $H_2MgSn_3S_8$, which are multi-valley indirect gap semiconductors. The calculated effective masses of carriers in these materials suggest high electron mobilities but lower hole mobilities due to their heavier masses. The carriers are confined to the $[MgSn_3S_8]^{2-}$ layer planes.

EXPERIMENTAL SECTION

Reagents. All starting elements were used as obtained unless stated otherwise: Sn powder (99.999% American Elements, Los Angeles, CA), sulfur buttons ground into powder (99.99%, 5 N Plus Inc., Saint-Laurent, Quebec, Canada), Mg powder (99% Sigma-Aldrich), Ni powder <50 μm (99.7% Sigma-Aldrich), Na_2CO_3 powder (>99.5% Sigma-Aldrich), and Na metal (99.9% Sigma-Aldrich). Na_2S was prepared using condensed ammonia, as reported previously.[27] ACS reagent grade HNO_3 70% (Sigma-Aldrich), ACS reagent grade HCl 70% (Sigma-Aldrich), and ACS reagent grade H_2SO_4 95−98% (Sigma-Aldrich). Amines used were ethylenediamine (≥99% Sigma-Aldrich), 1,12-diaminododecane (98% Sigma-Aldrich), 3-Picolylamine (≥99% Sigma-Aldrich), and Aniline (≥99.5% Sigma-Aldrich).

Solid-State Synthesis of $Na_2MgSn_3S_8$. Stoichiometric amounts of Sn powder (0.4748 g, 0.004 mol), S powder (0.3206 g, 0.01 mol), Na_2S powder (0.1561 g, 0.002 mol), and Mg powder (0.0486 g, 0.002 mol) were massed in an N_2 glovebox and loaded into a graphite crucible. The crucible was then placed into a 15 mm fused silica tube, which was evacuated to 5×10^{-3} mbar, and flame sealed. The sealed tube was heated to 800 °C at a rate of 100 °C/h, soaked at this temperature for 5 h, and then cooled to room temperature at a rate of 10 °C/h. The resulting product comprised of many plate-like crystals stuck together with an apparent dark color. When the crystals were separated, each one appeared translucent and bright yellow. Ground powder samples also had a yellow color. The materials were characterized by powder X-ray diffraction (PXRD), secondary electron microscopy−energy-dispersive X-ray spectroscopy (SEM-EDS), and differential thermal analysis (DTA).

Hydrothermal Synthesis of $Na_{2x}Mg_{2y-x}Sn_{4-y}S_8$. Stoichiometric amounts of Sn powder (4.7475 g, 0.04 mol), S powder (4.0615 g, 0.127 mol), Mg powder (0.4861 g, 0.02 mol), and Na_2CO_3 powder (2.1194 g, 0.02 mol) were combined in a 23 mL Teflon cup with 1.5 mL of DI water. The cup was then covered with a lid and sealed in a stainless-steel Parr autoclave. This autoclave was heated in an oven at 220 °C for 24 h. The autoclave was opened, and the contents were added to a 400 mL glass beaker with ∼200 mL of DI water. This solution was mixed and vacuum filtered, with an undissolved sediment and byproducts left in the beaker and discarded. The wet filter cake was then redispersed in ∼200 mL of acetone and filtered again, with any remaining undissolved sediment and byproducts left in the beaker discarded. The dry filter cake was then ground with an agate mortar and pestle until a homogenous powder remained. The yield was ∼80%. The resulting powder was bright yellow in color. The materials were characterized by PXRD, SEM-EDS, Fourier transform infrared−attenuated total reflectance (FTIR-ATR) spectroscopy, and Raman spectroscopy.

Hydrothermal Synthesis of Na_2SnS_3 (Equivalent to $Na_4[Na_{1.33}Sn_{2.67}]S_8$). Stoichiometric amounts of Sn powder (4.5503 g, 0.038 mol), S powder (4.0976 g, 0.128 mol), and Na_2CO_3 powder (4.0627 g, 0.038 mol) were combined in a 23 mL Teflon cup with 1.5 mL of DI water. The cup was then covered with a lid and sealed in a stainless steel Parr autoclave. This autoclave was heated in an oven at 220 °C for 24 h. The autoclave was opened, and the contents were added to a 400 mL glass beaker with ∼200 mL of DI water. This solution was mixed and vacuum filtered, with undissolved sediment and byproducts left in the beaker and discarded. The wet filter cake was then redispersed in ∼200 mL of acetone and filtered again, with any remaining undissolved sediment and byproducts left in the beaker discarded. The dry filter cake was then ground with an agate mortar and pestle until a homogenous powder remained. The yield was ∼80%. The resulting powder was bright yellow in color. The materials were characterized by PXRD, SEM-EDS, FTIR-ATR, and Raman spectroscopy. The difference in formula between Na_2SnS_3 (to be referred to as $Na_4[Na_{1.33}Sn_{2.67}]S_8$ stems from the different asymmetric units in the respective unit cells of their crystal structures.

Note of Caution in Conducting Stability Studies! Despite the fact that the NMS materials reported in this paper are stable in acid, as a general statement, when handling metal sulfides, we note the critical importance of safety precautions during stability studies due to potential H_2S formation, and to ensure this, all the reactions were conducted in a fume hood.

Acid Stability Study of $Na_{2x}Mg_{2y-x}Sn_{4-y}S_8$. 20 mL of multiple nitric acid solutions (0.1 M, 2 M, 4 M, 6 M) was added to four 20 mL glass vials with 0.3 g $Na_2MgSn_2S_6$. Each vial was shaken and allowed to sit for 4 h. Plastic dropper pipettes were then used to sample the powder at the bottom of each vial, which was added to glass microscope slides and allowed to dry overnight. When dry, the powder on each slide was scraped off with a razor blade and ground with a mortar and pestle. The materials were characterized by PXRD, FTIR-ATR, and SEM-EDS.

Acid Stability Study of $Na_{2x}Ni_{2y-x}Sn_{4-y}S_8$. 20 mL of multiple nitric acid solutions (0.1 M, 2 M, 4 M, 6 M) was added to four 20 mL glass vials with 0.2 g of $Na_2NiSn_2S_6$. Each vial was shaken and allowed to sit for 4 h. Plastic dropper pipettes were then used to sample the powder at the bottom of each vial, which was added to glass microscope slides and allowed to dry overnight. When dry, the powder on each slide was scraped off with a razor blade and ground with a mortar and pestle. The materials were characterized by PXRD and SEM-EDS.

Acid Stability Study of $Na_4[Na_{1.33}Sn_{2.67}]S_8$. 20 mL of multiple nitric acid solutions (0.1 M, 2 M, 4 M, 6 M) was added to four 20 mL glass vials with 0.2 g of $Na_4Sn_2S_6$. Each vial was shaken and allowed to sit for 4 h. Plastic dropper pipettes were then used to sample the powder at the bottom of each vial, which was added to glass microscope slides and allowed to dry overnight. When dry, the powder on each slide was scraped off with a razor blade and ground with a mortar and pestle. The materials were characterized by PXRD, FTIR-ATR, and SEM-EDS.

Preparation of Protonated Materials (Solid Acids). An amount of 1 g of a given material was added to a vial containing 20 mL of 0.6 M HCl. The vial was closed and vigorously shaken every 5 min for 30 min. After this, the material was vacuum filtered and washed once with DI water and once with acetone. The resulting protonated materials were orange/red. The materials were characterized by PXRD, SEM-EDS, and Raman spectroscopy.

https://doi.org/10.1021/acs.inorgchem.3c02064
Inorg. Chem. 2023, 62, 15971−15982

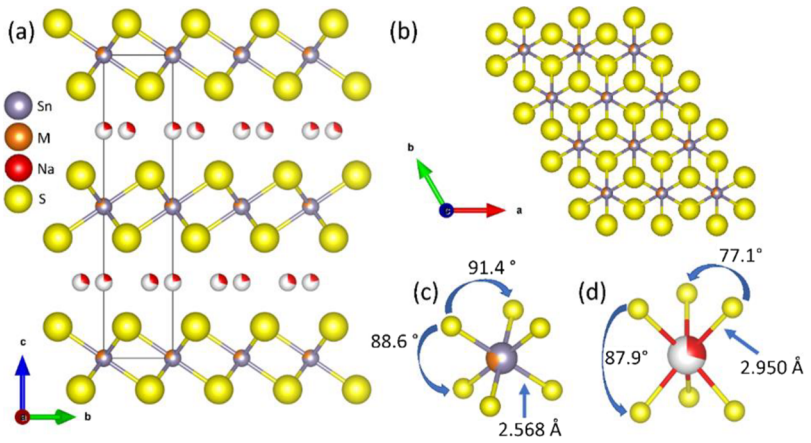

Figure 1. Crystal structure of $Na_2MgSn_3S_8$ oriented along the (a) [100] direction and (b) the [001] direction. Local coordination, bond lengths, and angles for (c) $(Sn/Mg)S_6$ octahedra and (d) NaS_6 trigonal prismatic.

Amine Acid–Base Reactions. 0.3 g of protonated material was added to a 20 mL glass vial along with the 2× stoichiometric excess of either aniline, ethylenediamine, 1,12-dodecanediamine, or 3-picolylamine. 20 mL of DI water was then added, and the vials were capped and thoroughly shaken. The vials were then allowed to sit for 1.5 h, with a thorough remixing performed after the first two half hours. A pasture pipette was then used to sample the powder from the bottom of the vial and added to a glass microscope slide for drying. After drying, the powder was scraped off the slide with a razor blade and ground with a mortar and pestle. The materials were characterized by PXRD, SEM-EDS, FTIR-ATR, and Raman spectroscopy.

Computational Details. To simulate the disordered structure of $Na_2MgSn_3S_8$, we constructed an ordered model of a 2 × 2 × 1 supercell (28 atoms) based on the refined structure of single crystal X-ray diffraction. Sn^{4+} and Mg^{2+} were arranged so that each $[MgS_6]^{10-}$ octahedron shares its edges with six $[SnS_6]^{8-}$ octahedra. This arrangement resulted in each $[SnS_6]^{8-}$ octahedron sharing its edges with two $[MgS_6]^{10-}$ and four $[SnS_6]^{8-}$ octahedra. We did the geometry optimization and calculated the total energy of these randomly generated supercells based on density functional theory (DFT) to find the one with the lowest total energy as the best approximation of disordered $Na_2MgSn_3S_8$. The structure of $H_2MgSn_3S_8$ was built subsequently by putting the H^+ at the same positions as Na^+ in $Na_2MgSn_3S_8$, followed by relaxing the structure. The calculations were performed using Vienna Ab initio Simulation Package (VASP)[28] implemented with projector augmented-wave (PAW) method.[29] We chose the generalized gradient approximation (GGA) of Perdew, Burke, and Ernzerhof (PBE)[30] as the exchange-correlation functionals with the cutoff energy of 500 eV for the plane-wave basis set. Lattices and atoms were fully relaxed until the energy difference between each two iteration steps was less than 10^{-6} eV, and the Hellmann-Feynman forces between any two atoms were less than 0.01 eV $Å^{-1}$. We adopted a Gamma-centered *k*-grid of 9 × 9 × 4 when performing the structure relaxation. A denser *k*-grid of 18 × 18 × 8 was used in Brillouin zone sampling for band structure and partial density of states (PDOS) calculation.

RESULTS AND DISCUSSION

Structure and Characterization. $Na_2MgSn_3S_8$, herein referred to as Mg-NMS, crystallizes in the space group $P6_3/mmc$ as a derivative of the 2-dimensional CdI_2 structure type, see Figure 1a,b, and is isostructural to other reported layered metal sulfides, namely $K_2MgSn_2S_6$ (KMS-2).[15] The structure was solved and refined using single crystal X-ray diffraction data collected on single crystals produced via a solid-state reaction. Selected crystallographic data are summarized in Tables 123. Each layer is defined by MS_6 edge-sharing octahedra, where Sn and Mg exhibit mixed occupancy on the M site, which are slightly compressed along the *c*-axis as the bond angle between S atoms on different sides of an individual layer are closer, 88.6°, than S atoms on the same side, 91.4°, see Figure 1c. In the refined structure, each sheet is anionic and carries a net −2 charge which is compensated by Na^+ atoms sitting in between the layers in a trigonal prismatic coordination, see Figure 1d. The mixed Mg/Sn occupancy on

Table 1. Single Crystal Data and Structure Refinement for $Na_2MgSn_3S_8$[a]

empirical formula	Mg Na2 S8 Sn3
formula weight	682.84
temperature	293(2) K
wavelength	0.71073 Å
crystal system	hexagonal
space group	$P6_3/mmc$
unit cell dimensions	a = 3.6770(5) Å, α = 90°b = 3.6770(5) Å, β = 90°c = 13.971(3) Å, γ = 120°
volume	163.58(6) $Å^3$
Z	0.5
density (calculated)	3.466 g/cm^3
absorption coefficient	7.025 mm^{-1}
$F(000)$	156
crystal size	0.2 × 0.2 × 0.1 mm^3
θ range for data collection	2.916–42.035°
index ranges	$-6 \le h \le 6$, $-6 \le k \le 6$, $-26 \le l \le 25$
reflections collected	7294
independent reflections	257 [R_{int} = 0.0438]
completeness to θ = 25.242°	100%
refinement method	full-matrix least-squares on F^2
data / restraints / parameters	257/1/12
goodness-of-fit	1.558
final R indices [$I > 2\sigma(I)$]	R_{obs} = 0.0267, wR_{obs} = 0.0773
R indices [all data]	R_{all} = 0.0269, wR_{all} = 0.0774
extinction coefficient	·
largest diff. peak and hole	1.376 and −0.707 e·$Å^{-3}$

[a] $R = \Sigma||F_o| - |F_c||/\Sigma|F_o|$, $wR = \{(\Sigma[w(|F_o|^2 - |F_c|^2)^2]/\Sigma[w(|F_o|^4)]\}^{1/2}$ and $w = 1/[\sigma^2(F_o^2) + (0.0248P)^2 + 0.4332P]$ where $P = (F_o^2 + 2F_c^2)/3$.

https://doi.org/10.1021/acs.inorgchem.3c02064
Inorg. Chem. 2023, 62, 15971−15982

Table 2. Atomic Coordinates ($\times 10^4$) and Equivalent Isotropic Displacement Parameters ($Å^2 \times 10^3$) for $Na_2MgSn_3S_8$ at 293(2) K, with Estimated Standard Deviations in Parentheses

label	x	y	Z	occupancy	U_{eq}[a]
Sn	10,000	0	5000	0.75	14(1)
S	6666.67	3333.33	3966(1)	1	14(1)
Na(1)	3333.33	6666.67	2500	0.294(15)	35(4)
Na(2)	0	10,000	2500	0.206(15)	40(7)
Mg	10,000	0	5000	0.25	14(1)

[a] U_{eq} is defined as one third of the trace of the orthogonalized U_{ij} tensor.

Table 3. Anisotropic Displacement Parameters ($Å^2 \times 10^3$) for $Na_2MgSn_3S_8$ at 293(2) K with Estimated Standard Deviations in Parentheses[a]

label	U_{11}	U_{22}	U_{33}	U_{12}	U_{13}	U_{23}
Sn	10(1)	10(1)	20(1)	5(1)	0	0
S	13(1)	13(1)	17(1)	6(1)	0	0
Na(1)	42(6)	42(6)	20(5)	21(3)	0	0
Na(2)	48(11)	48(11)	26(9)	24(5)	0	0
Mg	10(1)	10(1)	20(1)	5(1)	0	0

[a] The anisotropic displacement factor exponent takes the form: $-2\pi^2[h^2a^{*2}U_{11} + ... + 2hka^*b^*U_{12}]$.

the octahedral site within the layers was modeled by linking the occupancies of Mg and Sn and allowing them to refine freely. The refinement converged to a Mg/Sn ratio of 1:3, which was fixed and followed by free refinement of the Na occupancies employing a SUMP command to maintain charge neutrality. The bond lengths of the Sn/M−S bonds are 2.5680(7) Å which compares well with the Sn−S bond length in SnS_2 of 2.56(2) Å.[31] The Na−S bond length is 2.9496(8) Å which is slightly longer than the reported bond length in Na_2S of 2.83073(5) Å,[32] which reflects the partial occupancy of the Na^+ site in the structure.

The compound $Na_4Sn_2S_6$[26] or $Na_{5.33}Sn_{2.67}S_8$, herein referred to as Na-NMS, is isostructural to Mg-NMS with Na^+ atoms sitting in the Mg^{2+} sites. Layered metal sulfides can have different stacking sequences which lead to different formulas depending on the symmetry present. An example of this is KMS-1 ($K_2MnSn_2S_6$) vs KMS-2 ($K_{1.38}Mg_{0.69}Sn_{1.31}S_4$), where the difference originates from the A′-A-A′ stacking of KMS-2 vs the A-B-C-A sequence of KMS-1.[15] While Na-NMS crystallizes in space group $R\bar{3}m$ and Mg-NMS in $P6_3/mmc$, this alone does not account for the differences in formula between it and $Na_2MgSn_3S_8$. The culprit is that the ratio of Sn to M when M is Mg is 3:1, but when M is Na, it is 2:1. As mentioned above, formula for Na-NMS can be rewritten as $Na_4[Na_{1.33}Sn_{2.67}]S_8$, where the Na in brackets sits on the same site and shares occupancy with Sn. The net charge of each octahedral layer in the compound is then −4, where the rest of the sodium resides in between the octahedral layers to charge compensate. We analogously define the nickel analogue, with general formula $Na_{2x}Ni_{2y-x}Sn_{4-y}S_8$, as Ni-NMS.

The PXRD patterns of the pristine materials are presented in Figure S1a. They are characterized by a basal Bragg reflection, the (002), at 9.84 and 9.78° 2θ for Mg-NMS and Na-NMS, respectively. The (002) plane bisects the (Sn/Mg) atoms in the octahedral layers within the structure and directly corresponds to the interlayer spacing. The d-spacings of the hydrothermally prepared Mg-NMS and Na-NMS basal (002) reflections are 8.98 and 8.87 Å, respectively. The d-spacing values of the (002) reflections for both materials are larger than that observed in the solid state for Mg-NMS, 6.99 Å (12.66° 2θ). This expansion is attributed to the inclusion of water molecules in between the layers which solvate the Na^+ cations yielding a difference in d-spacing between 1.99 and 1.85 Å. Additional extents of hydration beyond the phase with $d_{(002)}$ = ∼9 Å are observed in hydrothermally produced products, indicating a d-spacing of ∼11.67 Å for the (002) suggesting an additional layer of H_2O in the structure, see Figure 2.

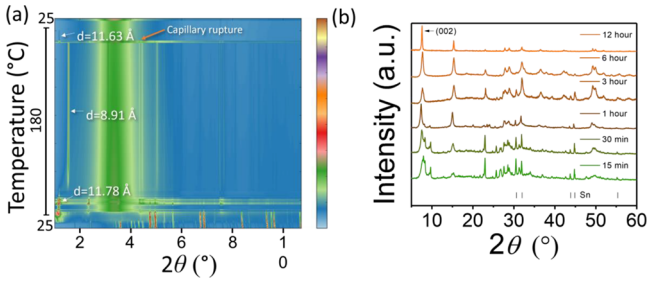

Figure 2. (a) Synchrotron in situ X-ray diffraction synthesis of $Na_{2x}Mg_{2y-x}Sn_{4-y}S_8$, (b) ex-situ variable dwell time reactions.

During hydrothermal synthesis, Mg-NMS forms quickly, see Figure 2b, with the appearance of the (002) reflection observed in the 15 min dwell reaction. At early timescales, multiple reflections occur near the (002) basal reflection corresponding to layered intermediate phases, which gradually decreases in intensity as the dwell time increases. Distinct among them is a reflection that occurs at ∼9.7° 2θ with a d-spacing of 9.10 Å in the 15 min dwell reaction. The difference in the d-spacing of this (002) reflection with the d-spacing observed in the 12 h reaction is ∼2.57 Å. Given that the size of a water molecule is ∼1.5 Å across,[33] this suggests that this and the nearby reflections are associated with different extents of hydration. In the in-situ panoramic[34] diffraction experiment conducted, see Figure 2a, we observe the formation of the final $Na_{2x}Mg_{2y-x}Sn_{4-y}S_8$ (Mg-NMS) phase within 30 min, indicated by the occurrence of the basal reflection with a d-spacing of 11.78 Å. The material then smoothly contracts over the next 30 min reaching a d-spacing of 8.91 Å, a total change of ∼2.87 Å, which persists until capillary failure by way of vapor escape from flame-sealed end breakage, at which point the material quickly expands to a d-spacing of 11.63 Å.

The hydrothermal synthesis of these materials generally produced materials with particle sizes <5 μm, with compositions that typically have low incorporation of Mg, Na, or Ni, see Figure S1b−d. The composition of the hydrothermal product can be written as $Na_{2x}Mg_{2y-x}Sn_{4-y}S_8$ (x = 1−1.41; y = 0.43−1; 0.18 < $2y - x$ < 1) based on the analysis of SEM-EDS spectra. This formula emphasizes that Na can occupy both the octahedral site in the layers and the sites between them. The existence of multiple site options for Na results in a wide range of possible compositions with varying Na/Sn ratios. The synthesis of $Na_{4x}[Na_{1.33x}Sn_{4-1.33x}]S_8$ (x = 0.48−1) (Na-NMS) proceeds similarly and exhibits a range of compositions as well. The range of compositions accessible from hydrothermal reactions is thus wider than that obtained from the solid state method due to the use of lower

https://doi.org/10.1021/acs.inorgchem.3c02064
Inorg. Chem. 2023, 62, 15971−15982

temperatures and the relative solubilities of the reagents, which allow access to nonidealized stoichiometries.

Acid Stability and Topotactic Protonation. The stability of each material in nitric acid, as well as the stability of Mg-NMS and Na-NMS in hydrochloric acid, was studied via the batch method, see Figures 3 and 4.

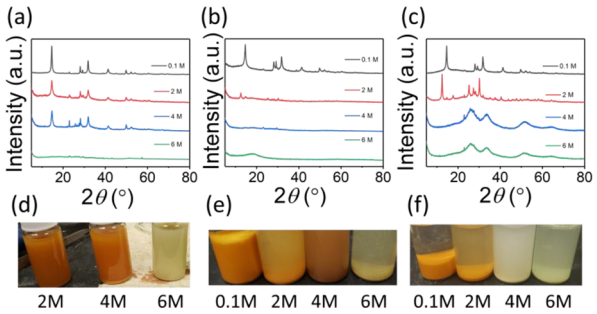

Figure 3. PXRD patterns and images of compounds submerged in HNO_3 solutions of $Na_{2x}Mg_{2y-x}Sn_{4-y}S_8$ (a) and (d), $Na_{2x}Ni_{2y-x}Sn_{4-y}S_8$ (b) and (e), and $Na_{5.33}Sn_{2.67}S_8$ (c) and (f).

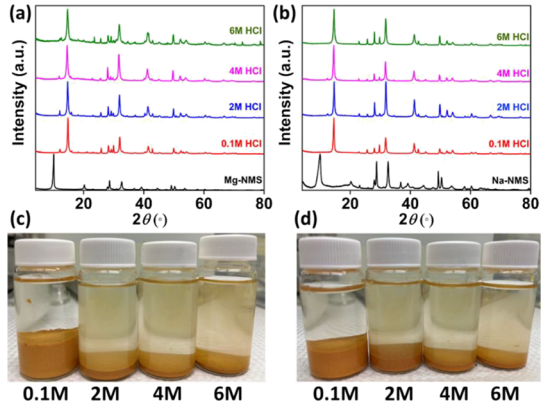

Figure 4. PXRD patterns of (a) $Na_{2x}Mg_{2y-x}Sn_{4-y}S_8$ and (b) $Na_{5.33}Sn_{2.67}S_8$ after 4 h of contact with HCl solutions. Optical images of the submerged (c) $Na_{2x}Mg_{2y-x}Sn_{4-y}S_8$ and (d) $Na_{5.33}Sn_{2.67}S_8$ in HCl solutions.

The three materials, Mg-NMS, Na-NMS, and Ni-NMS, were found to be stable in 0.1 M HNO_3 and undergo topotactic protonation and H^+/Na^+ exchange according to the chemical equations below. In addition, both Mg-NMS and Na-NMS formed the protonated Mg-HMS and Na-HMS after their immersion in 0.1 M HCl, and the resulting HMS materials remained stable for up to 4 days (Figure S2). Samples of Mg-NMS and Na-NMS, in addition to their protonated counterparts, analyzed via FTIR-ATR, see Figure S3, reveal the presence of absorption peaks near 2403 cm^{-1} which correspond to H−S stretching vibrations in the protonated materials which are unobserved before exposure to acid. SEM-EDS measurements on the protonated materials indicate a large reduction in the amount of Na present with approximate stoichiometries of "$Na_{0.06}Mg_{0.24}Sn_{3.68}S_8$" and "$Na_{0.19}Sn_{3.36}S_8$" for Mg-HMS and Na-HMS, respectively. The reactions presented thus far in addition to those that will be discussed in the subsequent sections are summarized in Figure 5.

Note that in the reaction for the protonation of Na-NMS, the Na_{int} refers to the Na^+ ions that are intercalated and the Na_{oct} refers to the ions that are part of the layers. This designation is made to emphasize that the Na^+ ions that are exchanged come predominantly from between the layers.

Mg-NMS.

$$Na_{2x}Mg_{2y-x}Sn_{4-y}S_8 + 2xHNO_3 \rightarrow H_{2x}Mg_{2y-x}Sn_{4-y}S_8 + 2xNaNO_3\ (x = 1 - 1.41;\ y = 0.43 - 1;\ 0.18 < 2y - x < 1) \quad (1)$$

Na-NMS.

$$(Na_{int,y}Na_{oct,y-1})_{5.33x}Sn_{4x}S_8 + yHNO_3 \rightarrow (H_yNa_{oct,1-y})_{5.33x}Sn_{4x}S_8 + yNa_{int}NO_3\ (x = 0.48 - 1) \quad (2)$$

Mg-NMS.

$$Na_{2x}Mg_{2y-x}Sn_{4-y}S_8 + 2xHCl \rightarrow H_{2x}Mg_{2y-x}Sn_{4-y}S_8 + 2xNaCl\ (x = 1 - 1.41;\ y = 0.43 - 1;\ 0.18 < 2y - x < 1) \quad (3)$$

Na-NMS.

$$(Na_{int,y}Na_{oct,y-1})_{5.33x}Sn_{4x}S_8 + yHCl \rightarrow (H_yNa_{oct,1-y})_{5.33x}Sn_{4x}S_8 + yNa_{int}Cl\ (x = 0.48 - 1) \quad (4)$$

In 2 M HNO_3 and 2 M HCl, Na-NMS and Mg-NMS survived, while complete decomposition of Ni-NMS was observed in a solution of 2 M HNO_3. Of note is that Na-HMS showed expansion along the *c*-axis in the 2 M solutions compared to the 0.1 M solutions, suggesting the inclusion of H_2O molecules into the interlayer space. In 4 M nitric acid, only Mg-HMS remained stable save for a noticeable reduction in the relative intensity of the (00*l*) family of basal reflections compared to the pattern at 0.1 M. This can be rationalized by the greater basicity of the Na-NMS compared to Mg-NMS. In addition, the stability of Na-HMS and Mg-HMS in solutions of 2 and 4 M HNO_3, respectively, was further confirmed by ICP-OES, where no leaching of metal has been observed. Furthermore, both Na-HMS and Mg-HMS were found to be stable in 4 M as well as in 6 M HCl for up to 4 days (Figure S2). The stability of these materials is high, as SnS_2 has been reported[35] to dissolve in 6 M HCl solutions in seconds. These results suggest that in acidic media, layered metal sulfides spontaneously undergo conversion into their protonated counterparts, but since HNO_3 is a powerful oxidizing agent, it may promote the oxidation of sulfide ligands and decomposition of the metal sulfide materials. In the presence of different acid concentrations, Ni-NMS demonstrated stability for 4 h in 0.1 M HNO_3, Na-NMS remained stable for 4 h in 2 M HNO_3, and the most resilient material, Mg-NMS, displayed stability for 4 h in 4 M HNO_3. Interestingly, both Na-HMS and Mg-HMS demonstrated notable stability in HCl solutions of 6 M for up to 4 days. However, although no Sn leaching has been observed for both HMS materials in 4 M HCl solutions, at solutions of 6 M HCl, the percentages of Sn leached for Na-HMS and Mg-HMS were calculated to be 15.5 and 15.1%, respectively.

In addition to HNO_3 and HCl, the stability of Mg-NMS and Na-NMS was examined in solutions of 0.1−6 M H_2SO_4 over

https://doi.org/10.1021/acs.inorgchem.3c02064
Inorg. Chem. 2023, 62, 15971−15982

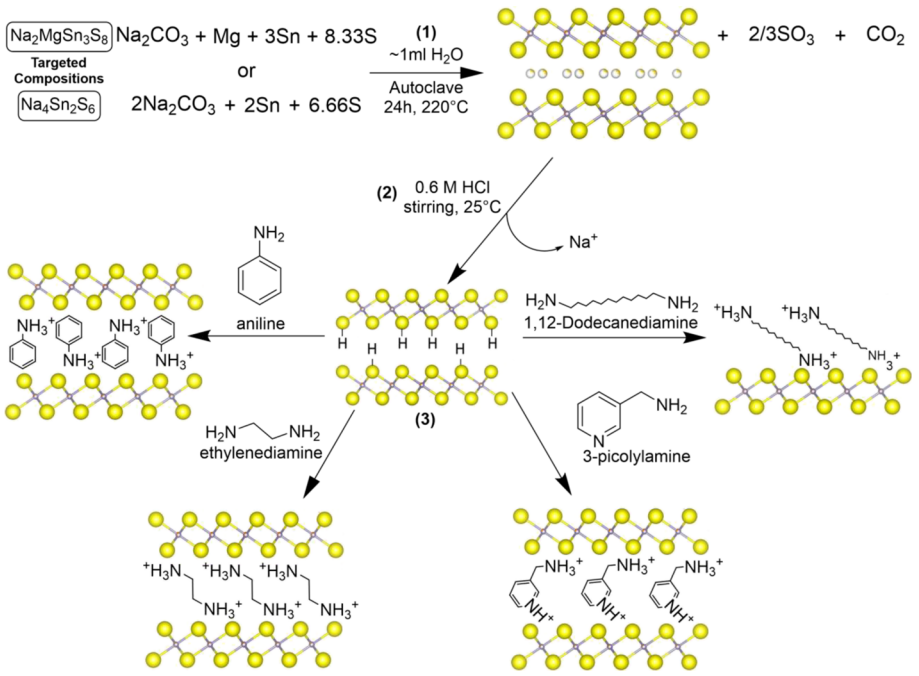

Figure 5. Reaction scheme summarizing (1) the syntheses of $Na_{2x}Mg_{2y-x}Sn_{4-y}S_8$ and $Na_{5.33}Sn_{2.67}S_8$, (2) preparation of the solid acid materials, and (3) reactions of solid acids with amines.

several hours to days (Figure S4). Surprisingly, when treated with 0.1 M H_2SO_4 for 4 h, the yellow color of NMS materials remained unchanged, indicating that the acidified materials retained their crystal structure as pristine compounds, with no exchange between Na^+ and H^+. Indeed, PXRD patterns of the acid-treated materials are quite similar to those of pristine materials (Figure S4). In addition, the FT-IR spectra of acidified materials show no H−S stretching peaks (Figure S5c). Solid samples collected from the orange-brown solutions of Mg-NMS and Na-NMS (in 2−6 M H_2SO_4) were not the protonated materials. PXRD patterns revealed expansion along the *c*-axis giving rise to the hypothesis that H_3O^+ and H_2O molecules are intercalated between the metal sulfide layers. Furthermore, FT-IR spectra of these solids displayed the characteristic absorption peak near 2400 cm^{-1} which is attributed to H−S stretching vibrations, suggesting the conversion of NMS to HMS. All the above advocate that the latter components are likely mixtures of HMS and NMS with H_2O/H_3O^+ intercalated between the layers. After 4 days of contact with the H_2SO_4, the expansion of the layers of Mg-NMS is even more noticeable, with the basal reflection found equal or close to 11.5 Å (Figure S5). Of note is that in the spectrum of Mg-NMS in 0.1 M H_2SO_4 appeared the characteristic peak of S−H bond at ∼2400 cm^{-1} (Figure S5), indicating that the latter is likely a mixture material, and the formation of Mg-HMS in 0.1 M H_2SO_4 is quite slower than in more concentrated solutions. In addition, TGA and GC−MS data revealed mass losses attributed to release of water molecules from the acid-treated material. Na-NMS after 4 days remains in a mixture of Na-NMS and Na-HMS in 2 and 4 M H_2SO_4 solutions but there is no evidence of the presence of Na-HMS in the 0.1 M H_2SO_4 solution. The PXRD pattern of Na-NMS in 6 M H_2SO_4 revealed that it was entirely converted to the protonated form, since the interlayer spacing was found to be 5.94 Å, a finding that was further confirmed by the EDS analysis. In conclusion, NMS materials fully retain their structural integrity in dilute (0.1 M) H_2SO_4 solution for treatment times up to 4 h, whereas formation of mixtures of pristine and protonated phases was observed for treatment with more concentrated sulfuric acid (2−6 M) or treatment with dilute H_2SO_4 solution for a longer period (up to 4 days). Although, H_2SO_4 is a "strong" acid, along with HNO_3 and HCl, the fact that it was not able to arouse the rapid protonation of NMS likewise to the other strong acids, is attributed to the dissociation of sulfuric acid in the water, accompanied by the constant production of H_3O^+ (along with the H^+) which intercalate between the NMS layers.

To better understand the formation of the protonated products, hereafter referred to as Mg-HMS and Na-HMS, we conducted time-resolved ion-exchange experiments tracked via PXRD to observe their formation, see Figure 6. The formation of Mg-HMS occurs quickly in less than an hour, see Figure 6a, forming a protonated phase with a contracted (002) reflection position of ∼5.97 vs 8.88 Å. This interlayer spacing is very similar to that of SnS_2 at 5.88 Å[31] and to previously reported $H_{2x}Mn_xSn_{3-x}S_6$[13] and corresponds to the unhydrated phase $H_{2x}Mg_{2y-x}Sn_{4-y}S_8$. Therefore, the layer structure motif is maintained, and the reaction can be classified as top-otactic.[36−38] We believe this is the phase present, as SEM-EDS measurements on ex-situ products confirm the presence of Mg in the ex-situ reaction products, see Figure S2, and the infrared spectrum indicates H−S stretches (see below). After forming, the protonated phase does not appear to change with additional contact time. Na-NMS behaves very differently compared to Mg-NMS when exposed to acid, as crystallinity decreases upon initial contact, as indicated by intensity loss peak broadening. The material slowly recovers its crystallinity over the course of several days and exhibits a contracted (002) reflection position compared to the pattern before exposure to acid, 5.99 vs 8.92 Å. This could be due to an exfoliation process that disrupts the layer stacking followed by restacking.

https://doi.org/10.1021/acs.inorgchem.3c02064
Inorg. Chem. 2023, 62, 15971−15982

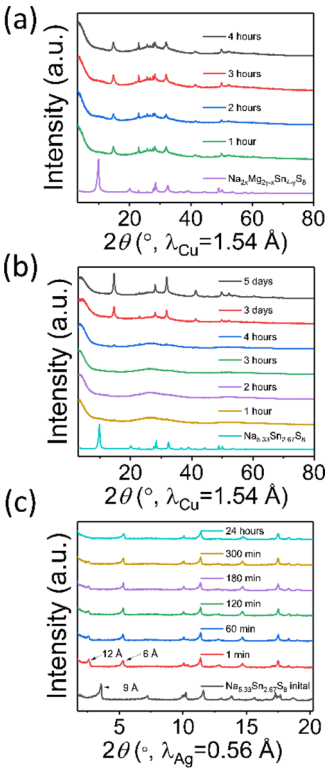

Figure 6. Time-resolved ex-situ PXRD patterns of materials in contact for (a) $Na_{2x}Mg_{2y-x}Sn_{4-y}S_8$ and (b) $Na_{5.33}Sn_{2.67}S_8$ in contact with 0.6 M HCl solutions. (c) In-situ PXRD patterns of $Na_{5.33}Sn_{2.67}S_8$ in contact with 2 M HNO_3 solutions.

The in-situ PXRD analysis of the conversion of Na-NMS to Na-HMS reveals a two-step conversion process. Upon first contact with acid, in <1 min, the material expands along the *c*-axis by ∼3 Å implying uptake of H_3O^+ in between the layers. After expansion, the intensity of the lowest angle reflection slowly begins to decrease until it is unobservable 24 h later, where a pattern identical to that observed in the ex-situ time-resolved experiment is reached. This behavior suggests that initially, the material expands to accept H_3O^+ in exchange for Na^+, and afterward, slowly expels H_2O leaving behind H^+ in the structure. The expulsion of H_2O is likely the reason for the slow conversion of the material over time. Interestingly, this behavior is only observed for $Na_4[Na_{1.33}Sn_{2.67}]S_8$ and may be a consequence of removing Na^+ ions from the octahedral layers themselves in addition to in between them, a process unavailable to the other materials studied.

Intercalation Reactions of Solid-Acids Mg-HMS and Na-HMS with Amines. In addition, the post-acidified products exhibit behavior characteristic of solid acids and are shown to react readily with amines. To investigate the ability of the Mg-HMS and Na-HMS to undergo acid−base reactions, we exposed them to a selection of organic amines and analyzed the reaction products via PXRD, see Figure 7.

The changes in d-spacing for their first basal reflections are summarized in Tables 4 and 5. Both materials readily reacted with available amines resulting in large expansions along their *c*-axis. These basal expansions indicated the protonation and subsequent intercalation of the amines in between the metal sulfide sheets. The extent of interlayer expansion is directly correlated to the size of the amine, the number of protonic sites on the molecule, and their spatial distribution. The

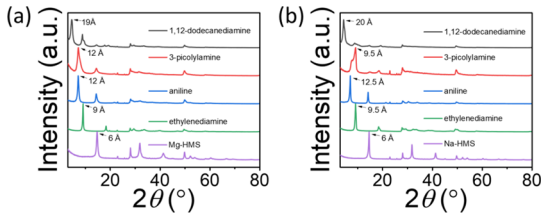

Figure 7. PXRD patterns of the products isolated after reacting (a) Mg-HMS and (b) Na-HMS with selected amines.

Table 4. Measured Bandgaps, Work Functions, and d-Spacing Values for Na-NMS and Its Derivatives

material/derivative	band gap (eV)	work function (eV)	d-spacing (Å)	Δ d-spacing (Å)
$Na_4[Na_{1.33}Sn_{2.67}]S_8$	2.42(5)	5.76(5)	8.83	
$H_4[Na_{1.33}Sn_{2.67}]S_8$	2.03(5)	5.75(5)	6.04	−2.79
aniline	1.88(5)	5.53(5)	12.45	3.62
3-picolylamine	2.08(5)	5.63(5)	11.38	2.55
ethylenediamine	1.98(5)	5.54(5)	9.54	0.71
1,12-dodecanediamine	2.24(5)	5.47(5)	19.85	11.02

Table 5. Measured Energy Bandgaps, Work Functions, and d-Spacing Values for Mg-NMS and Its Derivatives

material/derivative	band gap (eV)	work function (eV)	d-spacing (Å)	Δ d-spacing (Å)
$Na_{2.82}Mg_{0.18}Sn_{3.57}S_8$	2.40(5)	5.75(5)	8.95	
$H_xNa_{0.06}Mg_{0.24}Sn_{3.68}S_8$	2.30(5)	5.53(5)	6.03	−2.92
aniline	1.88(5)	5.68(5)	12.27	3.32
3-picolylamine	1.97(5)	5.62(5)	12.22	3.27
ethylenediamine	1.82(5)	5.67(5)	9.67	0.72
1,12-dodecanediamine	2.27(5)	5.49(5)	21.40	12.45

smallest interlayer expansion for both HMS materials is observed with ethylenediamine, as the amino groups lie on opposite ends of the short ethane backbone and likely bond to layers above and below them. In contrast, the reaction with aniline resulted in a larger d-spacing than ethylenediamine because it can only bond to one of its adjacent layers, necessitating a bilayer of anilinium ions to fully compensate all the charges. When reacted with 3-picolylamine, the resultant PXRD patterns were similar to the aniline analogs due to large structural similarities between these amines. The largest d spacing materials, at ∼19 to 20 Å were isolated with 1,12-dodecanediamine. This distance is smaller than the length of the amine from end to end, suggesting that the conformation of the molecule in between the layers is not straight but tilted or folded. Further analyses of the intercalated materials via FTIR-ATR spectroscopy confirmed the presence of the protonated amines within the materials evidenced by the presence of several characteristic vibrational modes, see Figures S6a S7a. SEM−EDX analysis confirmed the presence of nitrogen in each sample, see Figures S6b−e and S7b−e.

Optical Properties and Work Functions. The optical band gaps of both Mg-NMS, Na-NMS, and all their derivatives are presented in Figure 8a,b, respectively, and summarized in Tables 4 and 5. The band gaps of each parent material are almost identical at 2.40(5) eV for Mg-NMS and 2.42(5) eV for Na-NMS. This result is similar to the values for other reported layered metal sulfides based on SnS_2[16,39−41] and is identical to the bandgap of $K_2MgSn_2S_6$ (KMS-2).[15] Upon protonation, the

https://doi.org/10.1021/acs.inorgchem.3c02064
Inorg. Chem. 2023, 62, 15971−15982

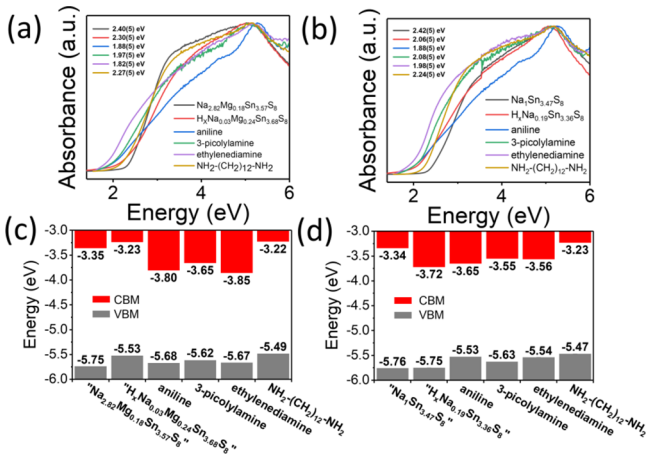

Figure 8. Normalized UV−vis absorbance spectra (derived via Kubelka−Munk equation, $F(R) = (1 - R)^2/2R$, from diffuse reflectance measurements) of (a) Mg-NMS and its derivatives and (b) Na-NMS and its derivatives. CBM and VBM band alignment plots for (c) Mg-NMS family and (d) Na-NMS family.

band gaps of both materials redshift to 2.30(5) eV for Mg and 2.06(5) eV for Na due to forming a covalent H−S bond, which replaces the ionic Na^+−S^{2-} bond. The difference in the magnitude of the reduction can be explained by noting that Mg^{2+} has a higher charge density than Na^+, which results in a more covalent contribution to the M−S bond within the layers. The overall red-shift in the bandgap can also be rationalized by the smaller electronegativity difference between H^+ and S^{2-} than between Na^+ and S^{2-}. Moreover, the increased covalency of the Mg−S bond leads to a lower electron density on S compared to the Na−S analog, resulting in a weaker H−S bond formation in the case of Mg compound. This fact explains why the reduction in band gap upon protonation is larger for Na-HMS, 0.36(5) eV, compared to Mg-HMS, 0.10(5) eV.

In the Raman spectra collected on the NMS and HMS compounds, see Figure S8a,b, the main feature near 300 cm^{-1} corresponds to the A_{1g} mode associated with Sn−S ring vibrations.[42−44] General features common to both the Mg and Na compounds include some peak asymmetry about the main Raman feature, a small shoulder extending above 300 cm^{-1} attributed to contributions from SnS_2-like modes, and a reduction in the force constant and peak full width at half-maximum (FWHM) upon protonation. In both Mg-NMS and Na-NMS, a lowering of the vibrational energy is observed upon conversion to their HMS counterparts because of the formation of covalent H−S bonds that inductively weaken the Sn−S bonds. Notably the decrease is much larger in Na-HMS, which is consistent with our observations of a greater reduction in the band gap compared to Mg-HMS.

When the Na-HMS and Mg-HMS react with selected amines, the band gaps relative to the pristine materials are similarly redshifted between 0.13 and 0.58(5) eV for $(R{-}NH_3)_{2x}Mg_{2y-x}Sn_{4-y}S_8$ and 0.18−0.54(5) eV for $(R{-}NH_3)_{y-1}Na_y)_4[Na_{1.33}Sn_{2.67}]S_8$. Of the amines tested, aniline and ethylenediamine produced the smallest gaps for both materials tested, with band gaps within the range of 1.82(5) − 1.98(5) eV. 3-picolylamine follows with a slightly larger band gap of 1.97(5) and 2.08(5) eV likely due to its slightly larger size. These shifts probably reflect the differences in hydrogen bonding strength between the ammonium ions and the sulfide ions in the layers ($R{-}NH_2{-}H^+\cdots S^{2-}$). The widest band gaps among the amines studied were achieved with 1,12-dodecandiamine, at 2.27(5) eV for Mg-NMS and 2.24(5) eV for Na-NMS and are due to the large steric bulk of the alkane backbone, which may hinder the ability of the terminal ammonium groups from maximally aligning themselves with the sulfide ions. The Raman spectra for all intercalation compounds are presented in Figure S8c,d.

Photoemission yield spectroscopy in air (PYSA)[45−48] spectra were collected on all studied materials from which the work functions of each material were extracted. PYSA measures the photoemission yield of electrons from a material's surface when it is irradiated with photons under ambient or atmospheric conditions. The technique provides information about the electronic properties of the material's surface, including its electron-occupied energy levels in the band structure. The work function of a semiconductor is equal to the negative value of the energy of the valence band maxima (VBM) with respect to vacuum such that $E_{WF} = -E_{VBM}$.

The energy of the conduction band minima (CBM) with respect to vacuum can be determined by combining the work function and the band gap through the relation: $E_{CBM} = E_g + E_{WF}$, where E_g is the bandgap. Note that defined in this manner, the E_{CBM} and E_{VBM} values are both negative in reference to the vacuum energy, which is defined as 0 eV. The derived band alignment plots for both the Mg-NMS and Na-NMS compounds and their derivatives are presented in Figure 8c,d, respectively. The CBM and VBM energy positions for the pristine materials are both nearly identical.

In the family of Mg-NMS derivatives, with the exception of 1,12-dodecanediamine, both the CBMs and VBMs move to lower energies with respect to the protonated materials with the CBMs lowering by 0.42−0.62(7) eV and the VBMs by 0.09−0.12(5) eV, see Figure 8c. For 1,12-dodecanediamine, the CBM and VBM rest near the same positions observed in Mg-HMS, differing by 0.01(7) and 0.04(5) eV. In the Na-NMS family, both the CBMs and VBMs move up relative to Na-HMS by 0.07−0.49(7) and 0.12−022(5) eV, respectively, see Figure 8d. Of note is that the band extrema of the Mg-HMS amine derivatives move toward slightly lower energies (i.e. farther from vacuum) relative to their positions in Mg-HMS. In the case of the Na-HMS amine derivatives, the opposite trend is observed with the extrema of the bands moving higher in energy (i.e. closer to vacuum).

Electronic Structure Calculations of Mg-NMS and Mg-HMS. We performed DFT calculations to analyze the electronic structure of $Na_2MgSn_3S_8$ and its protonated solid-acid counterpart. It is noteworthy that we used approximated models with ordered Na ions and therefore, the ordered models show orthorhombic and triclinic symmetry due to the symmetry reduction. The calculated band structures are depicted in Figure 9a,b, and the orbital-decomposed PDOS plots are shown in Figure 10. $Na_2MgSn_3S_8$ and $H_2MgSn_3S_8$ both have multi-valley featured band edges, with much flatter valence band edges than the conduction band edge. Both compounds are formally indirect gap semiconductors. However, multiple valence bands exist in both electronic structures with maxima of very closely lying energies (designated by the letters a-f in Figure 9a,b). In $Na_2MgSn_3S_8$, the bottom of the conduction band lies in the Γ point and the top of the valence band in the middle of the Γ−*Y* direction in the Brillouin zone, whereas in $H_2MgSn_3S_8$, it occurs in the middle of the Γ−*V* direction, as shown in Figure 9a,b. The

https://doi.org/10.1021/acs.inorgchem.3c02064
Inorg. Chem. 2023, 62, 15971−15982

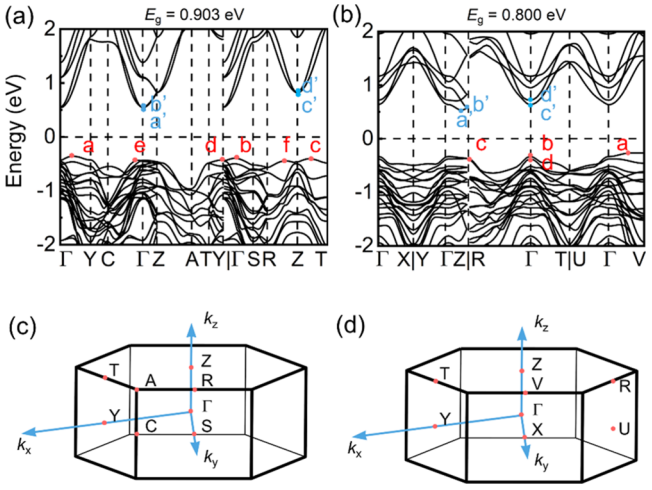

Figure 9. (a) Band structure of $Na_2MgSn_3S_8$ ordered structure with valence (conduction) band extrema marked alphabetically from a to f (a′ to d′). (b) Band structure of $H_2MgSn_3S_8$ ordered structure with valence (conduction) band extrema marked alphabetically from a to d (a′ to d′). (c) Brillouin zone of monoclinic $Na_2MgSn_3S_8$ ordered structure. (d) Brillouin zone of triclinic $H_2MgSn_3S_8$ ordered structure.

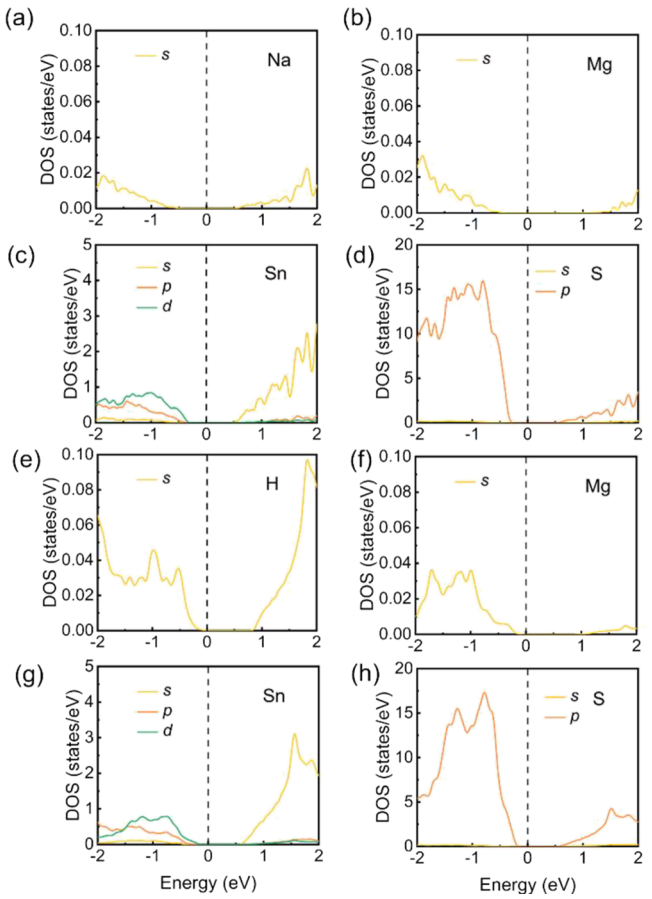

Figure 10. Orbital-specific partial density of states of (a) Na 3*s* orbital, (b) Mg 3*s* orbital, (c) Sn 4*d*, 5*s*, and 5*p* orbitals, (d) S 3*s* and 3*p* orbitals in $Na_2MgSn_3S_8$. Partial density of states of (e) H 1*s* orbital, (f) Mg 3*s* orbital, (g) Sn 4*d*, 5*s*, and 5*p* orbitals, (h) S 3*s* and 3*p* orbitals in $H_2MgSn_3S_8$.

PDOS plots shown in Figure 10a–d indicate that the valence band of $Na_2MgSn_3S_8$ is mainly contributed by the *p*–*p* and *p*–*d* orbital hybridization between S and Sn, while the *s*–*p* orbital hybridization dominates the conduction band. Na and Mg barely contribute to the band edge due to their ionic characteristics. $H_2MgSn_3S_8$, in comparison, has a part of valence band edge contribution from the *s*–*p* orbital hybridization between H and S, as shown in Figure 10e,h.

The formation of covalent H–S bonds dilutes the electron density around the Sn and S, leading to a weaker Sn–S bonding and, thus smaller energy difference between the bonding and anti-bonding orbitals. Given that Sn–S bonding and anti-bonding orbitals in $H_2MgSn_3S_8$ still have a dominant contribution to the highest occupied molecular orbital (HOMO) and the lowest unoccupied molecular orbital (LUMO), respectively, this eventually results in the narrower bandgap of $H_2MgSn_3S_8$. We calculated effective masses near the band extrema for electrons and holes to assess the potential for useful charge carrier properties of these materials. The energy level and corresponding single-band effective masses of each of the band extrema in $Na_2MgSn_3S_8$ and $H_2MgSn_3S_8$ are listed in Table 6. In $Na_2MgSn_3S_8$, VBM is located at the path between Γ and *Y*, with a large single band effective mass *m** of 2.48 m_0 (m_0 is the static mass of the free electron). Five other secondary VBM are distributed around the Γ point and Brillouin zone boundary (marked alphabetically with the energy in Figure 9) with *m** ranging from 0.90 to 3.26 m_0. The energy difference between these secondary VBM and the real VBM is small, ranging from 0.03 to 0.08 eV, which indicates that they tend to converge energetically and contribute to hole transport jointly. The CBM of $Na_2MgSn_3S_8$ is located at the center of the Brillouin zone. In fact, the Γ point has two conduction bands that nearly degenerate with very similar *m** (0.68 and 0.66 m_0). There is also a higher-lying secondary CBM at the *Z* point (0.27 eV above CBM) which also shows two-band-degenerated features with even lighter *m** of 0.51 and 0.50 m_0.

Table 6. Energy Level and Single Band Effective Masses of Band Extrema in $Na_2MgSn_3S_8$ and $H_2MgSn_3S_8$

$Na_2MgSn_3S_8$			$H_2MgSn_3S_8$		
band extrema	energy level (eV)	single band effective mass (m_0)	band extrema	energy level (eV)	single band effective mass (m_0)
a	−0.358	2.48	*a*	−0.266	5.37
b	−0.397	1.97	*b* (*G*)	−0.363	0.65
c	−0.405	2.25	*c* (*R*)	−0.373	3.63
d (*Y*)	−0.405	3.26	*d* (*G*)	−0.377	0.60
e	−0.427	0.90	*a*′	0.535	0.54
f	−0.434	2.08	*b*′ (*Z*)	0.557	0.42
a′ (*G*)	−0.545	0.68	*c*′ (*G*)	0.638	0.63
b′ (*G*)	−0.557	0.66	*d*′ (*G*)	0.820	0.66
c′ (*Z*)	−0.820	0.51			
d′ (*Z*)	−0.820	0.50			

In $H_2MgSn_3S_8$, the VBM emerges at the Γ–*V* path with a much larger *m** of 5.37 m_0 than the VBM of $Na_2MgSn_3S_8$. One of the secondary VBMs at the *R* point also shows a large *m** of 3.63 m_0. But the two secondary VBMs at the Γ point present much lighter *m** of 0.65 and 0.60 m_0, respectively, with a small energy difference of 0.01 eV. Similar to the Na analogue, the CBM of $H_2MgSn_3S_8$ lies between the Γ and *Z* point with *m** of 0.54 m_0. A lighter secondary CBM is located at the R point with *m** of 0.42 m_0. Two other secondary CBMs located at the

https://doi.org/10.1021/acs.inorgchem.3c02064
Inorg. Chem. 2023, 62, 15971−15982

Brillouin zone center showed m^* of 0.63 and 0.66, respectively, with an energy difference of 0.18 eV.

Because of the 2D nature of these structures, the carriers in these materials are confined in the planes of the $[MgSn_3S_8nS]$ layers. The light electron effective masses in both materials are comparable to other well known semiconductors such as SnS_2 (0.64 m_0),[49] 2D InS (0.26 m_0),[50] and $CuInS_2$ (0.16 m_0)[51] and suggest high electron mobilities and facile transport of carriers. The holes are considerably heavier and are expected to exhibit lower mobilities. However, the hole mobilities at the Brillouin zone center in the solid acid version $H_2MgSn_3S_8$ are predicted to be higher because of the significantly lower effective masses.

CONCLUSIONS

The layered $Na_{2x}Mg_{2y-x}Sn_{4-y}S_8$ (Mg-NMS) and $Na_4[Na_{1.33}Sn_{2.67}]S_8$, (Na-NMS) materials are highly stable in HNO_3 solutions, showing no degradation for 4 h in solution. Moreover, both NMS are able to exchange Na^+/H^+ in 0.1−6 M HCl, and the exchanged HMS materials were found to be stable for up to 4 days. In addition, in solutions of 0.1−6 M H_2SO_4, the slow protonation of HMS materials is accompanied by the formation of NMS materials with H_3O intercalated molecules. Upon contact with acid, the materials exchange their Na^+ ions for H^+ in solution in <15 min and form active solid acids that can participate in acid−base reactions. This property opens new potential avenues for testing these materials to treat highly acidic waste streams like those found in spent fuel rod reprocessing. In addition, the materials are also interesting nearly-direct semiconductors with bandgaps in the range of 2.40(5) and 2.42(5) eV with predicted attractive charge transport properties. The electronic structure of the 2D $Na_2MgSn_3S_8$ and $H_2MgSn_3S_8$ indicates that both compounds are indirect gap semiconductors with multi-valley featured band edges. The effective masses of the carriers were calculated to assess their potential for useful charge transport properties. The carriers in these materials are confined to the planes of the $[MgSn_3S_8]^{2-}$ layers. The light electron effective masses suggest high electron mobilities and facile transport of carriers, but the holes are considerably heavier and are expected to exhibit lower mobilities. By careful choice of amine base, the band gap of the protonated materials may be tuned between 1.88(5) and 2.27(5) eV, with the resulting optical gap being largely influenced by the nature of $[Sn_2S_6]$/R−NH_3 interactions, which allows for a facile way to tune the properties of intercalated metal sulfides. The solid acid Mg-HMS and Na-HMS materials are capable of intercalative protonation reactions with neutral amines forming a new class of layered organic hybrid materials.

ASSOCIATED CONTENT

Supporting Information

The Supporting Information is available free of charge at https://pubs.acs.org/doi/10.1021/acs.inorgchem.3c02064.

Additional experimental details, and methods, including SEM/EDS, PXRD, FT-IR, and Raman spectra (PDF)

Accession Codes

CCDC 2263492 contains the supplementary crystallographic data for this paper. These data can be obtained free of charge via www.ccdc.cam.ac.uk/data_request/cif, or by emailing data_request@ccdc.cam.ac.uk, or by contacting The Cambridge Crystallographic Data Centre, 12 Union Road, Cambridge CB2 1EZ, UK; fax: +44 1223 336033.

AUTHOR INFORMATION

Corresponding Author

Mercouri G. Kanatzidis − *Department of Chemistry, Northwestern University, Evanston, Illinois 60208, United States; Materials Science Division, Argonne National Laboratory, Lemont, Illinois 60439, United States;* orcid.org/0000-0003-2037-4168; Email: m-kanatzidis@northwestern.edu

Authors

Michael A. Quintero − *Department of Chemistry, Northwestern University, Evanston, Illinois 60208, United States;* orcid.org/0000-0002-0709-1676

Anastasia D. Pournara − *Department of Chemistry, Northwestern University, Evanston, Illinois 60208, United States;* orcid.org/0000-0002-5202-7032

Richard Godsel − *Department of Chemistry, Northwestern University, Evanston, Illinois 60208, United States*

Zhi Li − *Materials Science Division, Argonne National Laboratory, Lemont, Illinois 60439, United States;* orcid.org/0000-0003-0451-567X

Shobhana Panuganti − *Department of Chemistry, Northwestern University, Evanston, Illinois 60208, United States*

Xiuquan Zhou − *Department of Materials Science and Engineering, Northwestern University, Evanston, Illinois 60208, United States*

Christopher Wolverton − *Materials Science Division, Argonne National Laboratory, Lemont, Illinois 60439, United States;* orcid.org/0000-0003-2248-474X

Complete contact information is available at: https://pubs.acs.org/10.1021/acs.inorgchem.3c02064

Author Contributions

[‖]M.A.Q. and A.D.P. contributed equally.

Notes

The authors declare no competing financial interest.

$Na_2MgSn_3S_8$ CSD deposition number 2263492.

ACKNOWLEDGMENTS

This synthesis and material characterization study was supported by the Department of Energy's Nuclear Energy University Program (NEUP) through project 21-24188. R. Godsel acknowledges support from the Northwestern University for an undergraduate research Fellowship. This study made use of IMSERC at the Northwestern University, which has received support from the Soft and Hybrid Nanotechnology Experimental (SHyNE) Resource (NSF ECCS-1542205), the State of Illinois, and IIN. This study used the EPIC facility of Northwestern University's NUANCE Center, which has received support from the SHyNE Resource (NSF ECCS-2025633), the IIN, and the Northwestern MRSEC program (NSF DMR-1720139). Elemental analysis was performed at the Northwestern University Quantitative Bio-element Imaging Center, generously supported by the NIH under Grant S10OD020118. The synthetic aspects of this work were supported in part by National Science Foundation Grant DMR-2305731.

REFERENCES

(1) Paiva, A.; Malik, P. Recent advances on the chemistry of solvent extraction applied to the reprocessing of spent nuclear fuels and radioactive wastes. *J. Radioanal. Nucl. Chem.* **2004**, *261*, 485−496.

(2) Kolarik, Z. Complexation and separation of lanthanides (III) and actinides (III) by heterocyclic N-donors in solutions. *Chem. Rev.* **2008**, *108*, 4208−4252.

(3) Hubscher-Bruder, V.; Haddaoui, J.; Bouhroum, S.; Arnaud-Neu, F. O. Recognition of some lanthanides, actinides, and transition-and heavy-metal cations by N-donor ligands: thermodynamic and kinetic aspects. *Inorg. Chem.* **2010**, *49*, 1363−1371.

(4) Fryxell, G. E.; Mattigod, S. V.; Lin, Y.; Wu, H.; Fiskum, S.; Parker, K.; Zheng, F.; Yantasee, W.; Zemanian, T. S.; Addleman, R. S.; Liu, J.; Kemner, K.; Kelly, S.; Feng, X. Design and synthesis of self-assembled monolayers on mesoporous supports (SAMMS): The importance of ligand posture in functional nanomaterials. *J. Mater. Chem.* **2007**, *17*, 2863−2874.

(5) Tranter, T., Solid-phase extraction technology for actinide and lanthanide separations in nuclear fuel reprocessing. In *Advanced Separation Techniques for Nuclear Fuel Reprocessing and Radioactive Waste Treatment*; Elsevier: 2011; pp. 377−413.

(6) Donald, I.; Metcalfe, B.; Taylor, R. The immobilization of high level radioactive wastes using ceramics and glasses. *J. Mater. Sci.* **1997**, *32*, 5851−5887.

(7) Manos, M. J.; Kanatzidis, M. G. Metal sulfide ion exchangers: superior sorbents for the capture of toxic and nuclear waste-related metal ions. *Chem. Sci.* **2016**, *7*, 4804−4824.

(8) Manos, M. J.; Iyer, R. G.; Quarez, E.; Liao, J.; Kanatzidis, M. G. $\{Sn\ [Zn_4Sn_4S_{17}]\}^{6-}$: A Robust Open Framework Based on Metal-Linked Penta-Supertetrahedral $[Zn_4Sn_4S_{17}]^{10-}$ Clusters with Ion-Exchange Properties. *Angew. Chem. Int. Ed.* **2005**, *117*, 3618−3621.

(9) Manos, M. J.; Chrissafis, K.; Kanatzidis, M. G. Unique pore selectivity for Cs^+ and exceptionally high NH_4^+ exchange capacity of the chalcogenide material $K_6Sn[Zn_4Sn_4S_{17}]$. *J. Am. Chem. Soc.* **2006**, *128*, 8875−8883.

(10) Manos, M. J.; Ding, N.; Kanatzidis, M. G. Layered metal sulfides: exceptionally selective agents for radioactive strontium removal. *Proc. Natl. Acad. Sci. U. S. A.* **2008**, *105*, 3696−3699.

(11) Manos, M. J.; Kanatzidis, M. G. Highly efficient and rapid Cs^+ uptake by the layered metal sulfide $K_{2x}Mn_xSn_{3-x}S_6$ (KMS-1). *J. Am. Chem. Soc.* **2009**, *131*, 6599−6607.

(12) Manos, M. J.; Kanatzidis, M. G. Sequestration of heavy metals from water with layered metal sulfides. *Chem. − Eur. J.* **2009**, *15*, 4779−4784.

(13) Manos, M. J.; Petkov, V. G.; Kanatzidis, M. G. $H_{2x}Mn_xSn_{3-x}S_6$ (x= 0.11−0.25): A Novel Reusable Sorbent for Highly Specific Mercury Capture Under Extreme pH Conditions. *Adv. Funct. Mater.* **2009**, *19*, 1087−1092.

(14) Manos, M. J.; Kanatzidis, M. G. Layered metal sulfides capture uranium from seawater. *J. Am. Chem. Soc.* **2012**, *134*, 16441−16446.

(15) Mertz, J. L.; Fard, Z. H.; Malliakas, C. D.; Manos, M. J.; Kanatzidis, M. G. Selective Removal of Cs^+, Sr^{2+}, and Ni^{2+} by $K_{2x}Mg_xSn_{3-x}S_6$ (x= 0.5−1)(KMS-2) Relevant to Nuclear Waste Remediation. *Chem. Mater.* **2013**, *25*, 2116−2127.

(16) Sarma, D.; Malliakas, C. D.; Subrahmanyam, K.; Islam, S. M.; Kanatzidis, M. G. $K_{2x}Sn_{4-x}S_{8-x}$ (x= 0.65−1): a new metal sulfide for rapid and selective removal of Cs+, Sr^{2+} and UO_2^{2+} ions. *Chem. Sci.* **2016**, *7*, 1121−1132.

(17) Gupta, K.; Yuan, B. L.; Chen, C.; Varnakavi, N.; Fu, M. L. $K_{2x}Mn_xSn_{3-x}S_6$ (x=0.5-0.95) (KMS-1) immobilized on the reduced graphene oxide as KMS-1/r-GO aerogel to effectively remove Cs^+ and Sr^{2+} from aqueous solution. *Chem. Eng. J.* **2019**, *369*, 803−812.

(18) Li, J. R.; Wang, F. K.; Xiao, H.; Xu, L.; Fu, M. L. Layered chalcogenide modified by Lanthanum, calcium and magnesium for the removal of phosphate from water. *Colloids Surf., A* **2019**, *560*, 306−314.

(19) Li, J. R.; Wang, X.; Yuan, B. L.; Fu, M. L. Layered chalcogenide for Cu^{2+} removal by ion-exchange from wastewater. *J. Mol. Liq.* **2014**, *200*, 205−212.

(20) Li, J. R.; Xu, L.; Fu, M. L.; Lan, H. C. Can adsorbent of layered chalcogenide be regenerated? A case study of norfloxacin adsorbed by layered chalcogenide in water. *Colloids Surf., A* **2018**, *537*, 287−293.

(21) Li, J. R.; Xu, L.; Fu, M. L.; Wang, Y. X.; Xiao, H. Towards magnetic responsive chalcogenides for efficient separation in water treatment: facile synthesis of magnetically layered chalcogenide Fe_3O_4/KMS-1 composite adsorbents and their zinc removal application in water. *Inorg. Chem. Front.* **2018**, *5*, 403−412.

(22) Jiang, Z. Z.; Liu, G. L.; Ma, C.; Guo, Y. F.; Duo, J.; Li, M. L.; Deng, T. L. Cesium removal from wastewater: High-efficient and reusable adsorbent $K_{1.93}Ti_{0.22}Sn_3S_{6.43}$. *Chemosphere* **2022**, *305*, 135406.

(23) Jiang, Z. Z.; Ma, C.; He, Y. Q.; Li, M. L.; Liu, G. L.; Guo, Y. F.; Ji, D.; Deng, T. L. Novel layered iron antimony thiostannate adsorbent of $K_{1.61}Fe_{0.04}Sb_{0.03}Sn_{3.1}S_7$ for cesium green recovery from geothermal water. *J. Cleaner Prod.* **2022**, *347*, 131332.

(24) Li, J. L.; Jin, J. C.; Zou, Y. M.; Sun, H. Y.; Zeng, X.; Huang, X. Y.; Feng, M. L.; Kanatzidis, M. G. Efficient Removal of Cs^+ and Sr^{2+} Ions by Granulous $(Me_2NH_2)_{(4/3)}(Me_3NH)_{(2/3)}Sn_3S_7$ ● $1.25H_2O$/Polyacrylonitrile Composite. *ACS Appl. Mater. Interfaces* **2021**, *13*, 13434−13442.

(25) Tang, J.-H.; Jin, J.-C.; Li, W.-A.; Zeng, X.; Ma, W.; Li, J.-L.; Lv, T.-T.; Peng, Y.-C.; Feng, M.-L.; Huang, X.-Y. Highly selective cesium (I) capture under acidic conditions by a layered sulfide. *Nat. Commun.* **2022**, *13*, 658.

(26) Mark, W.; Lindqvist, O.; Jumas, J.-C.; Philippot, E. The OD structure of Na_2SnS_3. Determination and refinement of an MDO structure. *Acta Crystallogr., Sect. B: Struct. Sci.* **1974**, *30*, 2620−2628.

(27) Khoury, J. F.; Hao, S.; Stoumpos, C. C.; Yao, Z.; Malliakas, C. D.; Aydemir, U.; Slade, T. J.; Snyder, G. J.; Wolverton, C.; Kanatzidis, M. G. Quaternary Pavonites $A_{1+x}Sn_{2-x}Bi_{5+x}S_{10}$ (A^+= Li^+, Na^+): Site Occupancy Disorder Defines Electronic Structure. *Inorg. Chem.* **2018**, *57*, 2260−2268.

(28) Kresse, G.; Furthmüller, J. Efficient iterative schemes for ab initio total-energy calculations using a plane-wave basis set. *Phys. Rev. B* **1996**, *54*, 11169.

(29) Blöchl, P. E. Projector augmented-wave method. *Phys. Rev. B* **1994**, *50*, 17953.

(30) Perdew, J. P.; Burke, K.; Ernzerhof, M. Generalized gradient approximation made simple. *Phys. Rev. Lett.* **1996**, *77*, 3865.

(31) Hazen, R. M.; Finger, L. W. The crystal structures and compressibilities of layer minerals at high pressure; I, SnS< 2, berndtite. *Am. Mineral.* **1978**, *63*, 289−292.

(32) Bertheville, B.; Low, D.; Bill, H.; Kubel, F. Ionic conductivity of Na_2S single crystals between 295 and 1350 K experimental setup and first results. *J. Phys. Chem. Solids* **1997**, *58*, 1569−1577.

(33) Fortes, A. D.; Wood, I. G.; Grigoriev, D.; Alfredsson, M.; Kipfstuhl, S.; Knight, K. S.; Smith, R. No evidence for large-scale proton ordering in Antarctic ice from powder neutron diffraction. *J. Chem. Phys.* **2004**, *120*, 11376−11379.

(34) Shoemaker, D. P.; Hu, Y.-J.; Chung, D. Y.; Halder, G. J.; Chupas, P. J.; Soderholm, L.; Mitchell, J.; Kanatzidis, M. G. In situ studies of a platform for metastable inorganic crystal growth and materials discovery. *Proc. Natl. Acad. Sci. U. S. A.* **2014**, *111*, 10922−10927.

(35) Sorum, C.; Wolf, H. The solubilities of the sulfides of arsenic, antimony, and tin in hydrochloric acid. *J. Chem. Educ.* **1950**, *27*, 614.

(36) Krokidis, X.; Raybaud, P.; Gobichon, A.-E.; Rebours, B.; Euzen, P.; Toulhoat, H. Theoretical study of the dehydration process of boehmite to γ-alumina. *J. Phys. Chem. B* **2001**, *105*, 5121−5130.

(37) Lou, X. W.; Deng, D.; Lee, J. Y.; Feng, J.; Archer, L. A. Self-supported formation of needlelike Co_3O_4 nanotubes and their application as lithium-ion battery electrodes. *Adv. Mater.* **2008**, *20*, 258−262.

(38) Rivest, J. B.; Jain, P. K. Cation exchange on the nanoscale: an emerging technique for new material synthesis, device fabrication, and chemical sensing. *Chem. Soc. Rev.* **2013**, *42*, 89−96.

(39) Friedrich, D.; Quintero, M. A.; Hao, S.; Laing, C. C.; Wolverton, C.; Kanatzidis, M. G. A $InSn_2S_6$ (A= K, Rb, Cs)—

https://doi.org/10.1021/acs.inorgchem.3c02064
Inorg. Chem. 2023, 62, 15971−15982

Layered Semiconductors Based on the SnS_2 Structure. *Inorg. Chem.* **2022**, *61*, 13525.
(40) Pogu, A.; Vidyasagar, K. Syntheses, structural variants and characterization of $A_2ZnSn_3S_8$ (A= Cs, Rb) and $A_2CdSn_3S_8$ (A= Cs, Rb, K, Na) compounds. *J. Solid State Chem.* **2020**, *291*, No. 121647.
(41) Sarma, D.; Islam, S. M.; Subrahmanyam, K.; Kanatzidis, M. G. Efficient and selective heavy metal sequestration from water by using layered sulfide $K_{2x}Sn_{4-x}S_{8-x}$ (x= 0.65−1; KTS-3). *J. Mater. Chem. A* **2016**, *4*, 16597−16605.
(42) Felton, J.; Blundo, E.; Kudrynskyi, Z.; Ling, S.; Bradford, J.; Pettinari, G.; Cooper, T.; Wadge, M.; Kovalyuk, Z.; Polimeni, A.; Beton, P.; Grant, D.; Walker, G.; Patanè, A. Hydrogen-Induced Conversion of SnS_2 into SnS or Sn: A Route to Create SnS_2/SnS Heterostructures. *Small* **2022**, *18*, 2202661.
(43) Mead, D.; Irwin, J. Raman spectra of SnS_2 and $SnSe_2$. *Solid State Commun.* **1976**, *20*, 885−887.
(44) Smith, A.; Meek, P.; Liang, W. Raman scattering studies of SnS_2 and $SnSe_2$. *J. Phys. C: Solid State Phys.* **1977**, *10*, 1321.
(45) Hadar, I.; Hu, X.; Luo, Z.-Z.; Dravid, V. P.; Kanatzidis, M. G. Nonlinear Band Gap Tunability in Selenium−Tellurium Alloys and Its Utilization in Solar Cells. *ACS Energy Lett.* **2019**, *4*, 2137−2143.
(46) Harwell, J. R.; Baikie, T.; Baikie, I.; Payne, J. L.; Ni, C.; Irvine, J. T. S.; Turnbull, G. A.; Samuel, I. D. W. Probing the energy levels of perovskite solar cells via Kelvin probe and UV ambient pressure photoemission spectroscopy. *Phys. Chem. Chem. Phys.* **2016**, *18*, 19738−19745.
(47) He, Y.; Stoumpos, C. C.; Hadar, I.; Luo, Z.; McCall, K. M.; Liu, Z.; Chung, D. Y.; Wessels, B. W.; Kanatzidis, M. G. Demonstration of energy-resolved γ-ray detection at room temperature by the $CsPbCl_3$ perovskite semiconductor. *J. Am. Chem. Soc.* **2021**, *143*, 2068−2077.
(48) Yamashita, D.; Ishizaki, A. In situ measurements of change in work function of Pt, Pd and Au surfaces during desorption of oxygen by using photoemission yield spectrometer in air. *Appl. Surf. Sci.* **2016**, *363*, 240−244.
(49) Xue, Y.; Zhou, W.; Ding, L.; Jiang, J.; Ning, H.; Liang, X.; Zhou, W.; Guo, J.; Huang, D. First-principles study on Sb-doped SnS_2 as a low cost and non-toxic absorber for intermediate band solar cell. *Phys. Lett. A* **2020**, *384*, No. 126695.
(50) Zhou, S.; Liu, C.-C.; Zhao, J.; Yao, Y. Monolayer group-III monochalcogenides by oxygen functionalization: a promising class of two-dimensional topological insulators. *npj Quantum Mater.* **2018**, *3*, 16.
(51) Shabaev, A.; Mehl, M.; Efros, A. L. Energy band structure of $CuInS_2$ and optical spectra of $CuInS_2$ nanocrystals. *Phys. Rev. B* **2015**, *92*, No. 035431.

https://doi.org/10.1021/acs.inorgchem.3c02064
Inorg. Chem. 2023, 62, 15971−15982